Graphene Induces Formation of Pores That Kill Spherical and Rod-Shaped Bacteria

Vy T. H. Pham,[†] Vi Khanh Truong,[†] Matthew D. J. Quinn,[†] Shannon M. Notley,[†] Yachong Guo,[‡] Vladimir A. Baulin,[‡] Mohammad Al Kobaisi,[†] Russell J. Crawford,[†] and Elena P. Ivanova*,[†]

[†]School of Science, Faculty of Science, Engineering and Technology, Swinburne University of Technology, Hawthorn, Melbourne 3122, VIC, Australia and [‡]Department d'Enginyeria Quimica, Universitat Rovira i Virgili, 26 Av. dels Paisos Catalans, 43007 Tarragona, Spain

ABSTRACT Pristine graphene, its derivatives, and composites have been widely reported to possess antibacterial properties. Most of the studies simulating the interaction between bacterial cell membranes and the surface of graphene have proposed that the graphene-induced bacterial cell death is caused either by (1) the insertion of blade-like graphene-based nanosheets or (2) the destructive extraction of lipid molecules by the presence of the lipophilic graphene. These simulation studies have, however, only take into account graphene–cell membrane interactions where the graphene is in a dispersed form. In this paper, we report the antimicrobial behavior of graphene sheet surfaces in an attempt to further advance the current knowledge pertaining to graphene cytotoxicity using both experimental and computer simulation approaches. Graphene nanofilms were fabricated to exhibit different edge lengths and different angles of orientation in the graphene sheets. These substrates were placed in contact with *Pseudomonas aeruginosa* and *Staphylococcus aureus* bacteria, where it was seen that these substrates exhibited variable bactericidal efficiency toward these two pathogenic bacteria. It was demonstrated that the density of the edges of the graphene was one of the principal parameters that contributed to the antibacterial behavior of the graphene nanosheet films. The study provides both experimental and theoretical evidence that the antibacterial behavior of graphene nanosheets arises from the formation of pores in the bacterial cell wall, causing a subsequent osmotic imbalance and cell death.

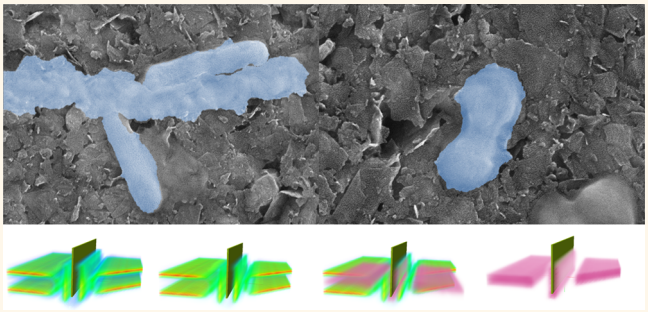

KEYWORDS: graphene nanosheet films · bactericidal effect · edge densities · pore formation · single mean field simulation

Graphene (GN) has been the focus of intensive research over the past decade with a rapidly expanding range of applications, including in electronics, energy, water, and biomedicine.[1−4] Recent studies have demonstrated that pristine graphene[5−7] and its derivatives[5−10] (for example, graphene oxide,[7,11,12] reduced graphene oxide (rGO),[1,8,13,14] quantum dots, or silver or polymer graphene composites[15−20]) may possess antibacterial properties. Graphene composites have also been shown to exhibit promising antiviral properties.[21,22] The mechanism by which these antimicrobial properties arise continues to be the subject of debate and is dependent also on the source of graphene and its chemical and physical properties. A few mechanisms have been suggested to explain the antibacterial mode of action of graphene, including the production of reactive oxygen species,[9] oxidative stress,[1,8] or the graphene directly extracting the phospholipid membranes of the bacteria in question.[10,12]

These discussions have principally been focused on the existence of two possible scenarios; one focuses on the action of the sharp edges of the graphene micro- or nanosheets, which act as "nano-knives" to cut through the cell membrane of bacteria, causing the leakage of intracellular substances and eventually causing cell death.[7,23] This mechanism is sometimes referred to as an "insertion mode" of action, which leads to membrane stress; this has been defined in several theoretical simulations and experimental studies.[7,23] For example, Akhavan reported that both GO and rGO exhibited bactericidal behavior toward Gram-negative *Escherichia coli* and Gram-positive

* Address correspondence to eivanova@swin.edu.au.

Received for review June 3, 2015 and accepted July 11, 2015.

Published online July 11, 2015
10.1021/acsnano.5b03368

© 2015 American Chemical Society

Staphylococcus aureus bacteria arising from the direct contact of the bacterial cell wall with the sharp edges of the GO and rGO.[7] Akhavan also reported the inactivation of bacteria by exposure to aggregated GO nanosheets through a trapping mechanism that prevented the bacteria from exchanging materials with the outer environment, preventing cell division.[24] The proposed mechanism of this insertion mode has been described in several computational simulations; however, some inconsistencies in the reported data have been noted. Li *et al.* suggested that the bactericidal action occurred through a spontaneous localized piercing of the bacterial cell wall by the sharp edges and corner sites present on the graphene microsheets, which is then followed by the full penetration of the graphene through the lipid bilayer.[23] Computer simulations have shown that the nearly orthogonal orientation of the sharp edges of the graphene sheets has the lowest interactive free energy with respect to the phospholipid bilayer of the bacteria, thus facilitating the most energetically favorable penetration configuration. These simulation results were supported by Yi *et al.*, who further reported that the insertion of the graphene sheets through the lipid bilayer was size-dependent, where the graphene microsheets preferred to adopt a near-perpendicular configuration in relation to the cell wall, while the nanosheets were required to adopt a position that was parallel to the lipid bilayer. This configuration was driven by the preferential attraction between the hydrocarbon tails of the lipids with the more lipophilic flat face of the graphene, allowing the graphene to sink in between the lipid tails, embedding the graphene nanosheet into the cell membrane.[25] These results, however, are in disagreement with the model proposed by Dallavalle, who demonstrated that, on a nanometer scale, the smaller the graphene sheets the more freely they could diffuse into the lipid membrane at a preferential perpendicular orientation, while larger nanosheets would prefer to arrange themselves across the membrane, embedding themselves into the more lipophilic section of the cell membrane.[26] It should be noted that, thus far, computer simulations have been poorly supported by the available experimental data.

The second postulated mechanism stipulates that the destructive effect of graphene on bacterial membranes is induced from the direct contact of bacterial cell membrane with the basal plane of graphene/graphene oxide.[6,11,12] The recent work of Li *et al.* showed that the destructive effect of graphene is derived from electron transfer from the bacterial cell membrane to the basal plane of the graphene.[12] Mangadlao *et al.* further demonstrated that the antimicrobial efficiency of graphene was not dependent on their sharp edges but relied upon the contact that took place between the GO basal planes and *Escherichia coli* K12 cells.[11] This group showed that an 89% *E. coli* killing efficiency could be achieved using a GO film that had been fabricated using the Langmuir–Blodgett deposition method, while eliminating the extent of exposure of the sharp edges present on the GO to the bacteria. The similar work performed by Hui and coworkers also demonstrated that masking of the GO basal plane decreased the antimicrobial efficiency of the GO nanosheets by decreasing the extent of direct contact between the *E. coli* and the basal plane of the GO.[12]

An additional possible mechanism for this behavior was proposed by Luan *et al.*,[27] who demonstrated that the flat face of the graphene nanosheets, being lipophilic, could disrupt the protein–protein bonding in the cell membrane, leading to the destabilization of the three-dimensional structure of the protein, causing its functional failure.[27] These researchers also reported the observation of a bacterial "self-killing effect", where the bacterial metabolic activity increased, causing the GO to be reduced to a form of graphene that was bactericidal *via* a glycolysis process.[28]

In this paper, the antimicrobial behavior of pristine graphene nanosheets was investigated in an attempt to further advance the current knowledge pertaining to graphene cytotoxicity using both experimental and computer simulation approaches. Graphene film surfaces, composed of multiple layers of graphene nanosheets, were analyzed for their roughness, edge density, stack orientation, and the effect that these parameters had with respect to bactericidal efficiency. A series of single-chain main field (SCMF) simulations of the interactions taking place between lipid bilayers and the graphene surfaces, where the distances between the respective edges of the graphene plates were varied, were also performed.

RESULTS AND DISCUSSION

Fabrication and Characterization of Graphene Films. Graphene was produced using a liquid-phase exfoliation procedure as previously described.[29,30] Subsequently, films of the graphene were produced using a vacuum filtration process, resulting in two different surface topographic characteristics on the top side of the filter and on the side facing the filter surface (Table 1). The two sides of the exfoliated graphene films exhibited different surface nanotopography in terms of their lateral dimensions, density, and orientation on the film surface (both surface types were used in comparative analyses, as shown in Figures S1 and S2, Supporting Information). The top surface of the film was designated as "graphene nanorough" (GN-R), and the surface facing the filter was referred to as "graphene nanosmooth" (GN-S). The X-ray diffractometry (XRD) pattern on the GN-R and GN-S surfaces demonstrated the existence of a significant reduction in the characteristic graphite ⟨002⟩ reflection at a 2θ of 27° in comparison to that of the graphite (GT) surfaces used as the control (Figure 1b).[31,32] The Raman spectra

TABLE 1. Topographical Analysis of Graphene (GT) and Rough (GN-R) and Smooth (GN-S) Graphene Surfaces over Scanning Areas of 2 μm × 2 μm

roughness parameters	GT	GN-R	GN-S
S_q (nm)	0.2 ± 0.1	58.9 ± 9.7	24.0 ± 1.4
S_a (nm)	0.1 ± 0.03	44.1 ± 8.4	18.5 ± 0.9
S_{max} (nm)	2.0 ± 0.6	618.0 ± 143.4	215.6 ± 29.7
S_{skw}	0.7 ± 0.05	0.10 ± 0.05	−0.7 ± 0.2
S_{kur}	5.6 ± 1.4	4.9 ± 1.9	4.1 ± 0.6
length of edge (nm) (L_{GN})[a]	n/a[a]	137.3 ± 93.9	79.7 ± 56.7
density of graphene edge length (μm/μm^2) (d_{edge})	0[b]	7.7	10.8
angle of GN sheet (deg) (θ_{GN})[b]	0	62.1	37.2

[a] Molecularly smooth surfaces were used as the reference without exposed edges. [b] GT surface used as the reference plane to measure the orientation angle of graphene sheet.

showed D, G, and 2D peaks at 1350, 1582, and 2700 cm^{-1}, indicating the presence of graphene on both film surface types (Figure 1c).[33−35] The relative height of the D peak in comparison to the G peak is characteristic of the edge defects and the single, symmetric 2D peak, confirming the presence of atomically thin graphene sheets. The graphene thickness estimation was derived from the ratio between the Raman intensity of the 2D band (~2700 cm^{-1}) and the G band (~1582 cm^{-1}).[33,36] The graphene sheets of both GN-R and GN-S were estimated to contain approximately 4 individual layers (I_{2D}/I_G ~ 0.3), each with a thickness of 1.4 nm. In Figure S1 (Supporting Information), the thickness of four layer graphene was confirmed by the shift in the 2D peak from 2744 cm^{-1} (graphite) to 2673 cm^{-1} (graphene).[37]

The stacking orientation of the graphene sheets resulted in a difference in the surface topography and architecture between the GN-R and GN-S films (Figure 2). AFM and SEM analysis indicated that the stacks of graphene sheets in the GN-S films were less than 1 μm in lateral size, whereas the stacks of graphene sheets present in the GN-R were greater than 1 μm in lateral size. The average size of the graphene stacks on the GN-R (top surface of the film) and GN-S (bottom surface of the film) was found to be 1.5 μm and 500 nm, respectively (Figure 2b,c). An AFM analysis of 1 μm × 1 μm scanning areas of provides statistical surface roughness parameters such as root-mean-squared roughness (S_q), average roughness (S_a), maximum roughness (S_{max}), skewness (S_{skw}), and kurtosis (S_{kur}). Other surface statistical parameters have been included in the Supporting Information. In comparison, the molecularly smooth graphite (GT) surfaces possessed a root-mean-squared roughness (S_q) of 0.2 ± 0.1 nm (Table 1). The differences in surface topography between the topside (GN-R) and bottom side (GN-S) of the graphene films produced during the filtration process, known as the "Brazil nut effect",[38,39] resulted in the geometrical reorganization of the graphene

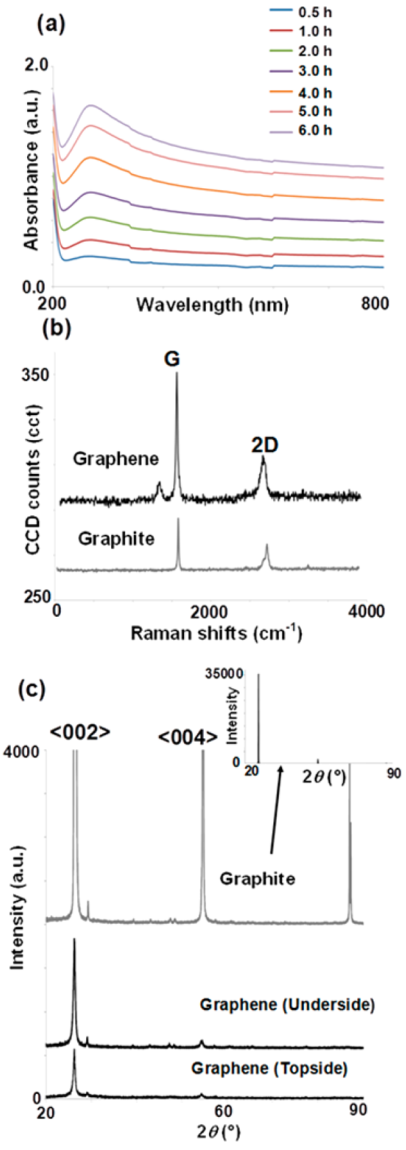

Figure 1. Characterization of the surfaces of graphite and graphene films. (a) Evolution of the UV−vis spectra of aqueous graphene suspensions during the 6 h exfoliation process; (b) X-ray diffractogram and (c) Raman spectra of GT, GN-S, and GN-R films.

sheets. As shown in the SEM and AFM images presented in Figure 2a,b, the GN-R surfaces had an S_q of 58.9 ± 9.7 nm, which was found to be (statistically significantly) more nanorough than the GN-S, which had an S_q of 24.0 ± 1.4 nm (Table 1). No significant differences were found between the other topographical parameters such as skewness and kurtosis for the GN-R and GN-S surfaces, indicating that the surface nanoarchitecture pattern of both graphene surfaces was very similar.

The distribution of the exposed graphene edges on both the GN-R and GN-S surfaces was analyzed using SEM (Figure 3a,b). The graphene edge length on the GN-R was estimated to be within the range 100−250 nm, whereas the edge length on the GN-S was found to be below 100 nm in most instances

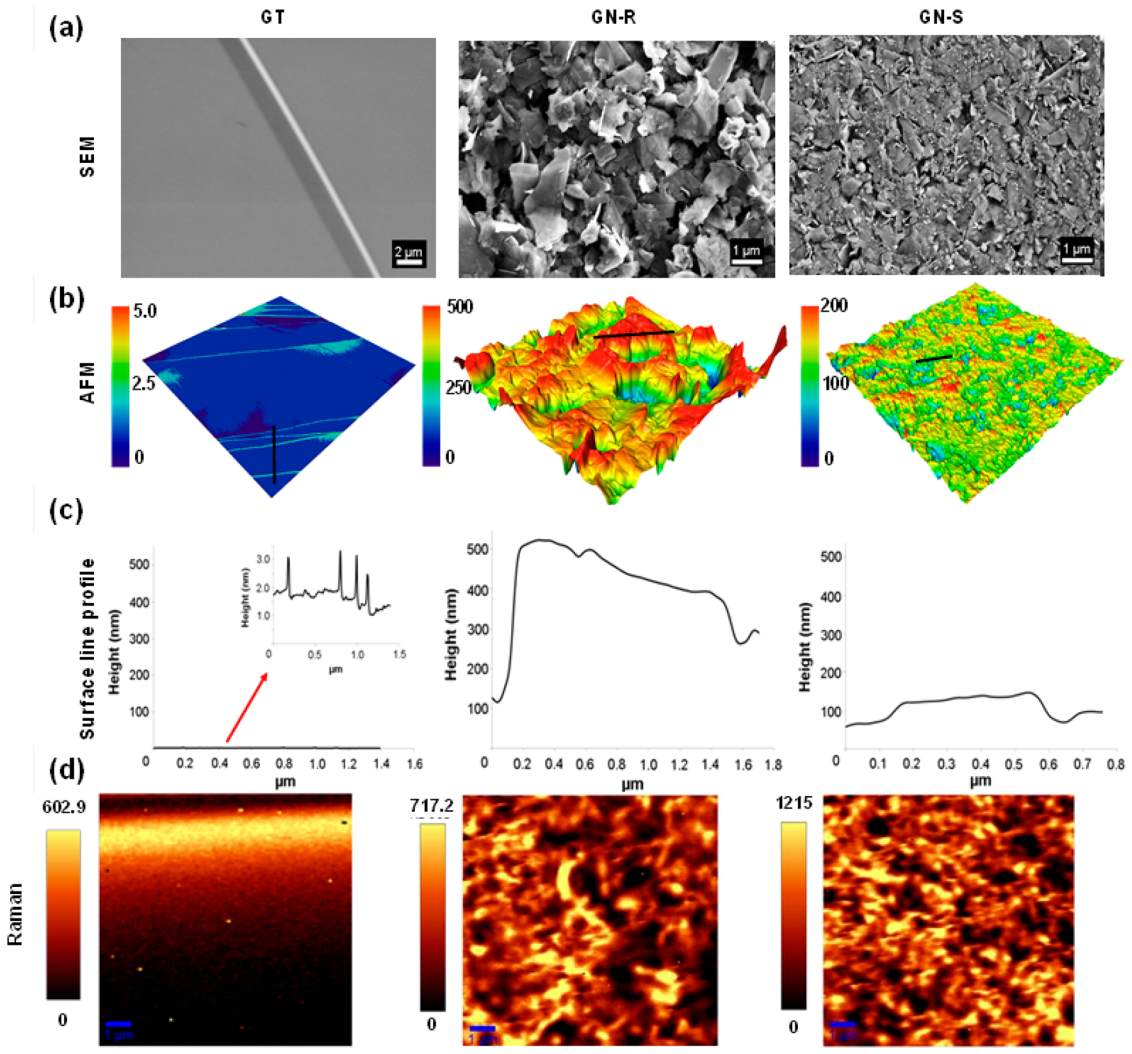

Figure 2. Surface topographies of the GT, GN-R, and GN-S films visualized using SEM, AFM, and Raman spectroscopy. This illustrates the typical geometry, size, and thickness of the graphite and graphene surfaces as a reflection of different dimensions in the arrangement of the graphene sheets. AFM images were taken over a scanning area of 5 μm $\times$ 5 μm, with the corresponding surface line profile representing the roughness of the graphite layers and graphene sheets.

(Figure 3c). The average length of the exposed edges was estimated to be 137 and 80 nm for the GN-R and GN-S, respectively (Table 1). Further analysis of the orientation of the graphene sheets was carried using AFM, with the graphite surface being used as the reference plane. It appeared that the stacks of graphene nanosheets on the GN-R and GN-S samples were oriented at 62.1° and 37.2°, respectively. The graphene edge length density was estimated to be 7.7 and 10.8 μm/μm^2 for the GN-R and GN-S surfaces, respectively.

Bactericidal Effect of Graphene Nanosheet Films. It was seen that *S. aureus* and *P. aeruginosa* bacterial cells were able to attach onto the two types of graphene and graphite surfaces (Figure 4a,b). Notably, however, the number of attached cells was variable among the substrates, with increased numbers of attached cells being observed on the surfaces with greater smoothness, *i.e.*, the molecularly smooth surfaces of pyrolytic graphite (GT). This observation is consistent with our previous investigations of bacterial attachment to glass, polymeric, and metallic surfaces of various degrees of surface nanoroughness, confirming once again that the nanotopography of a surface influences the degree of bacterial attachment, with a preference for nanosmooth surfaces.[40−44]

Analysis of the SEM and CLSM images clearly indicated that the two types of graphene surfaces were bactericidal toward both *S. aureus* and *P. aeruginosa*, whereas these cells remained viable on the GT film surfaces (Figures 4 and 5 and Figure S3, Supporting Information). The morphology of the bacterial cells was shown to be affected when they attached to the graphene surfaces (Figure 5 and Figure S3, Supporting Information). The results of the cell viability analysis (based on the fluorescent labeling of both live and dead cells) indicated that up to 87.6% of *P. aeruginosa* and 43.1% of *S. aureus* cells were dead on the GN-R film

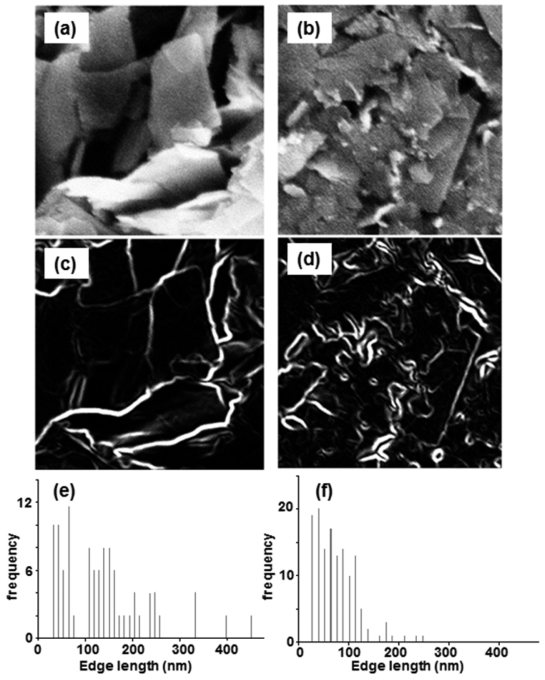

Figure 3. Distribution of the sharp edges of the graphene sheets on (a, c, e) GN-R and (b, d, f) GN-S surfaces. (a, b) Scanning electron micrograph showing the stacking order of the graphene nanosheets over a 1 μm $\times$ 1 μm area. (c, d) Contrast enhancement performed using SEM images to reveal the edge of the graphene nanosheets. (e, f) Distribution of the edge length on GN-R and GN-S graphene surfaces.

surfaces and 71.4% of *P. aeruginosa* and 77.1% *S. aureus* cells were dead on GN-S film surfaces (Figure 4c).

The variable bactericidal efficiency of the graphene micro- and nanosheet stacks formed on the GN-R and GN-S films requires further consideration. While the physicochemical characteristics of the GN-R and GN-S surfaces were the same (Table 1), three parameters were found to be different between the samples. These were the exposed edge length (L_{GN}), the angle of orientation of the graphene stacks (θ_{GN}), and the density of the graphene edge length (d_{edge}). It was seen that the GN-R surfaces, with an L_{GN} of 137.3 nm, d_{edge} 7.7 μm/μm^2, and θ_{GN} 62.1° were highly lethal to the *P. aeruginosa* cells (87.6% of cells killed) but less effective against the *S. aureus* (up to 53.1% of cells killed). Conversely, the GN-S surfaces, which are approximately five times more nanosmooth than the GN-R, with an L_{GN} 79.7 nm, d_{edge} 10.8 μm/μm^2, θ_{GN} 37.2°, exhibited a substantially greater bactericidal action against both types of bacterial cells (up to 70% of the cells being killed). Recently, it was reported that the differences in bactericidal efficiency may be due to the interactive angle of the exposed graphene edge with the bacterial cell membrane, with a maximum killing efficiency occurring at an orientation of 90° to the membrane surface.[1,5,13] Our experimental data indicated that graphene surfaces containing a 37° orientation remained effective at killing the bacteria. We therefore believe that the density of graphene edges (*e.g.*, GN-S films) is one of the main parameters that contributed to the bactericidal efficiency of graphene nanosheets films against both Gram-negative *P. aeruginosa* and Gram-positive *S. aureus* cells (Figures S3−S5, Supporting Information). It is likely that the decrease in the bactericidal efficiency of the GN-R against the *S. aureus* cells arises as a result of a combination of two factors: (i) the smaller, spherical *S. aureus* cells potentially use the larger graphene nanosheets as shelters, and (ii) the decreased density of graphene edges on these substrates allowed the cells to colonize the surface of the graphene nanosheets. Similar studies have demonstrated that the size of the graphene nanosheets can be responsible for the genotoxicity of eukaryotic cells;[45,46] however, there are no studies that have shown that different graphene sizes exhibit variable degrees of genotoxicity toward bacteria.

Interaction between the Bacterial Cell Membrane and Graphene Surfaces. Most of the studies simulating the interaction between bacterial cell membranes and the surface of graphene[10,23,47] have proposed that the graphene-induced bacterial cell death is caused either by (1) the insertion of blade-like graphene-based nanosheets[23,47] or (2) by the destructive extraction of lipid molecules by the presence of the graphene.[10] Li *et al.* also demonstrated the spontaneous penetration of graphene microsheets with single and a few layers in thickness into the lipid bilayer of bacterial cells. Their work revealed that membrane penetration begins with Brownian motion that includes the rotation, vibration and migration of the GN sheets into the bilayers, followed by the localized spontaneous piercing of the sheet corners into the tail groups of the lipids by attractive forces, subsequently allowing full penetration of the membrane.[23] These simulation studies, however, have only taken into account graphene-cell membrane interactions where the graphene is in a dispersed form.

To further simulate the interaction between bacterial cell membranes and graphene surfaces, we performed a series of single-chain main field (SCMF) simulations of the interaction between a lipid bilayer with the surface of the flat basal plane of graphene as a function of the distance between the respective edges of the graphene surface and a perpendicularly oriented lipid bilayer plane. To implement such a system, a simulation box containing the graphene surface was replicated with periodic boundary conditions. The structural rearrangement of lipids and the free energy cost of the insertion of the lipid-attractive graphene surface as a function of the distance from the center of the bilayer within the SCMF theory are shown in Figure 6. As is the case with the perpendicular insertion of hydrophobic carbon nanotubes into a lipid bilayer,[2]

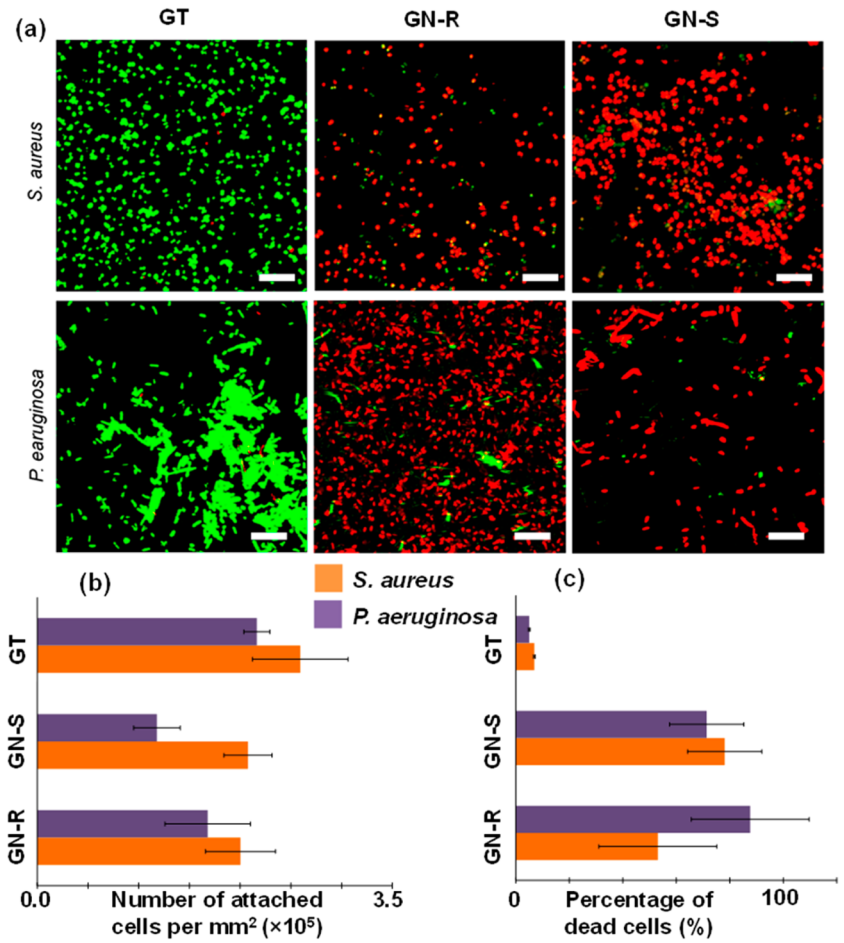

Figure 4. Typical (a) CLSM images and (b) quantification of bacterial cells attached to the surface and (c) the quantity of nonviable cells present on the GT, GN-R, and GN-S surfaces. Live cells are stained green; dead cells are stained red (scale bar 10 μm).

the minimum penetration energy is at half-insertion, *i.e.*, when the edge of the surface reaches the center of the hydrophobic core, which corresponds to a distance of 0 nm. This occurs as a result of the balance between a gain due to the insertion of a hydrophobic object into the core of the bilayer and the loss arising from the exposure of the edge to the solvent. The pattern on the surface consists of sheets that are treated as attractive truncated sheets of equal size and height, as shown in Figure 6. The width/thickness (w) of the cuboid was designated to be 3.3 Å. The sheets represent a forbidden zone for lipids, but the tails of the lipids present in the cell bilayer strongly interact with sheets with an interaction parameter of $\varepsilon_{obj} = -5$, -6, and -7.5 kT at distances shorter than 8.1 Å. An increase in the effective lipophilicity of the GN ($\varepsilon_{obj} = -5$, -6, and -7.5 kT) changes the characteristics of the interaction with the bilayer and the structural changes around the GN (Figure 6). It was experimentally confirmed that the antibacterial activity of the graphene was dependent on the degree of GN lipophilicity.[7]

As shown in Figure 6c, the surface of the bilayer can lift in order to attach to the GN sheet, increasing the area of contact between the GN and the hydrocarbon tails of the lipids. Full insertion of the GN sheet into the membrane leads to the formation of pores, the energy of which, together with the structure, strongly depends on the lipophilicity of the GN. In the least lipophilic case, the bilayer core is separated from the GN by the layer of head groups, while in the most lipophilic case, $\varepsilon_T = -7.5$ kT, the tails interact with the surface of the GN. The results of this simulation indicate that the surface of the graphene nanosheets do not act as a simple blade cutting through the cell membrane but rather act to induce the formation of pores within the cell membrane, altering the osmotic pressure in the bacterial cell, which causes them to swell and eventually die. This possible scenario was confirmed experimentally using confocal microscopy (Figure 7); the nonviable *S. aureus* cells present on the surface (stained with propidium iodide, red color) appeared to be much larger in size than the corresponding viable cells (stained with Syto 9, green color) (Figure 7).

CONCLUSIONS

A simple fabrication process was carried out to design and produce graphene nanofilms that contained different edge lengths and different angles of orientation of

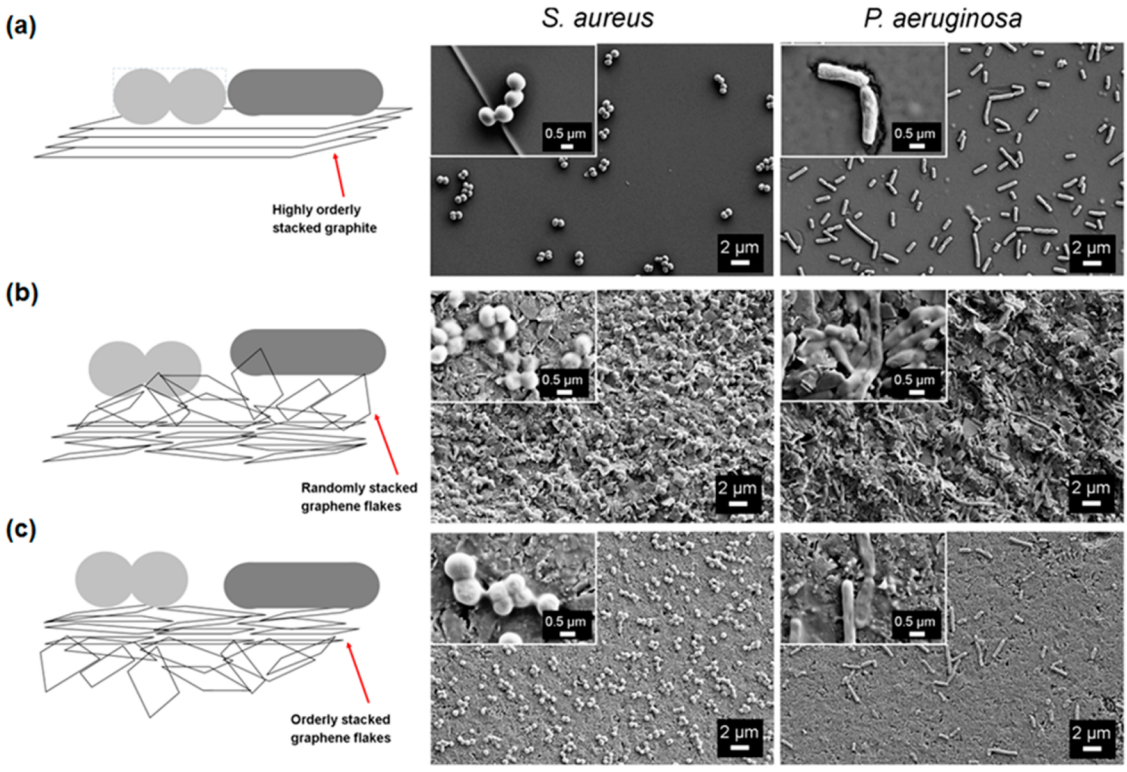

Figure 5. Typical attachment patterns of *S. aureus* and *P. aeruginosa* on GT, GN-R, and GN-S films with a schematic depiction of the interfacial interaction taking place between the bacteria and different three-dimensional arrangements of the GT and GN surfaces.

the graphene sheets. These substrates were placed in contact with *P. aeruginosa* and *S. aureus* bacteria, where it was seen that these substrates exhibited variable bactericidal efficiency toward these two pathogenic bacteria. It was demonstrated that the density of the edges of the graphene was one of the principal parameters that contributed to the antibacterial behavior of the graphene nanosheets. This provides both experimental and theoretical evidence that the antibacterial behavior of graphene nanosheets arises from the formation of pores in the bacterial cell wall, causing a subsequent osmotic imbalance and cell death.

METHODS

Graphene Sheet Exfoliation. Graphite powder and hexadecyltrimethylammonium bromide (CTAB) were purchased from Sigma-Aldrich. Graphene sheet films were fabricated using liquid-phase exfoliation followed by subsequent film formation as previously reported.[29,30] A suspension of graphene was exfoliated in an aqueous solution of CTAB. The surfactant assisted in the exfoliation by reducing the surface tension of the liquid phase to match the cohesive energy of graphite. The surfactant also inhibited reaggregation through adsorption onto the planar surface of the graphene. A stock solution of 0.6 mM CTAB was prepared in Milli-Q water by heating at 40 °C with continuous stirring for 30 min. The solution was preheated for 10 min prior to each experiment. Each sample was prepared by dispersing 10% graphite (w/v) in 0.6 mM CTAB. The exfoliation was performed *via* ultrasonication using a Q700 Qsonica (Qsonica, LLC, Newtown, CT) ultrasonicator at 60 W for 6 h. UV−vis absorption (Varian Cary 6000i UV−vis spectrophotometer) and ζ potential (the value of ζ potential was determined from the electrophoretic mobility using the Smoluchowski equation) (ZetaPALS; Brookhaven Instruments Corp.). Measurements of the suspension were taken every hour during the exfoliation process. The UV−vis spectra of the graphene suspension confirmed the presence of a highly conjugated arrangement of carbon atoms in graphene sheets with a peak in the absorption band at 270 nm (Figure 1a), which is in agreement with previously published work.[29,30] After 6 h of sonication, the solution was allowed to stand for 24 h to allow for the formation of any unstable aggregates and then centrifuged for 20 min at 1500 rpm (Eppendorf Centrifuge 5702). The supernatant was dialyzed against Milli-Q water for 2 days to remove excess CTAB using 0.02 μm cellulose dialysis tubing.

Graphene Film Fabrication. The dialyzed 200 mL solution was vacuum filtered through an alumina membrane (0.02 μm, Anapore, Whatman) with excess Milli-Q water used to remove any remaining traces of CTAB. When the resulting graphene film was completely dry, it was gently removed from the membrane. The section of the film that was furthest from the membrane was referred to as "GN-R", and the inner side (top side), closest to the membrane, was referred to as "GN-S" (bottom side). The absence of surfactant on the graphene surface was confirmed using energy dispersive X-ray spectroscopy (EDX) (Figure S2, Supporting Information). The absence of both nitrogen and bromine peaks in the surface scans confirm the complete removal of CTAB through the rinsing process. Highly oriented pyrolytic graphite (GT) was used as the control in all experiments. The surface was prepared by single peeling of the top layers of commercial graphite using Kapton tape (DuPont). The peeled graphite film was attached to a glass surface for handling during in all experiments.

Surface Characterization. The graphite, GN-R, and GN-S graphene films were systematically characterized. In order to

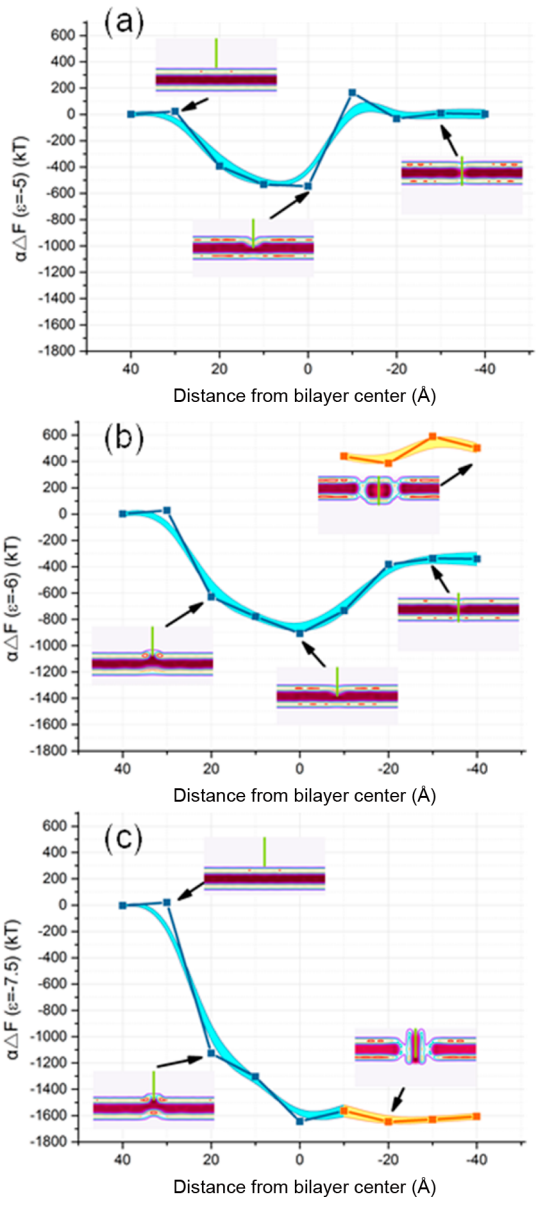

Figure 6. Free energy difference ΔF between the phospholipid bilayer and inserted graphene sheets with varying hydrophobicity (interaction parameter (ε_{obj}) of (a) -5, (b) -6, and (c) -7.5 kT) as a function of the distance from the bilayer center to the edge of the surface. Distance 40 corresponds to the unperturbed bilayer before the contact with the surface (zero energy, reference state); blue stripe corresponds to the solution of insertion of the surface into the bilayer with no change in the bilayer configuration; orange stripe corresponds to the solution with a pore in the bilayer (positive energy). Selected density profiles correspond to different positions of graphene surface; the colors of the bilayer represent the volume fraction of tails and heads from 0 to 1 (purple represents lipid tail and contour line represents lipid head).

understand the physicochemical properties of these surfaces, EDX (ZEISS SUPRA (Germany)) operated at 15 keV was used to determine the chemical composition of the films. A WiTEC Raman microspectrometer with a 532 nm laser wavelength ($h\nu$ = 2.33 eV) was used to confirm the identity of the graphite and graphene films. A single spectrum was acquired for each sample as an average of 100 spectra obtained from surrounding positions, with an integration time of 2 s. Surface scanning was

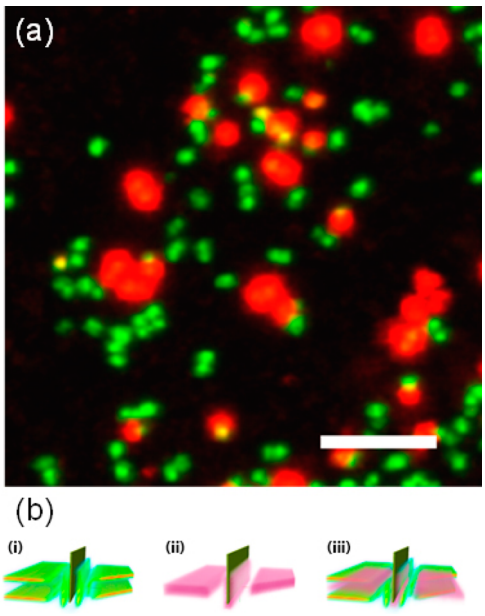

Figure 7. Interaction behavior between the bacterial cell membrane and graphene sheet. (a) Increase in size of nonviable *S. aureus* after the insertion of graphene sheet (green indicates viable cells; red is indicates nonviable cell with inserted graphene sheet) (scale bar 10 μm). (b) Three-dimensional snapshot of simulated interaction between graphene sheet and phospholipid membrane resulting in pore formation at interaction parameter (ε_{obj}) of -7.5 kT, from left (i) to right (iii): lipid head and graphene flake; lipid tail and graphene flake; both lipid head and tail with graphene flake.

performed on five different areas of every fabricated sample. The crystallinity of the films was investigated using the Bruker DiffracPLUS X-ray diffractometer (XRD) employing Cu $K\alpha$ radiation (λ = 0.15406 nm). The samples were scanned over a 2θ range of 30−85° at a scanning rate of 1 degree per minute. High-resolution SEM images of the graphite and graphene surfaces were taken using a FESEM (ZEISS SUPRA 40VP) at 3 kV under 5000, 10000, and 25000× magnification. AFM scans were conducted using an Innova scanning probe microscope (Veeco/Bruker, USA). Scans were performed in tapping mode at ambient temperature and pressure using silicon cantilevers with a spring constant of 0.9 N m^{-1} and a resonance frequency of approximately 20 kHz. Scanning was performed perpendicular to the axis of the cantilever at a scan speed of 1 Hz. Four scanning areas each of 10 μm × 10 and 1 μm × 1 μm area of clean and undamaged subsections of the substrate surface were performed.

The quantitative topographical analysis of the SEM images was carried out using ImageJ software (NIH USA Image ver. 1.61). Initially, SEM images were band-pass filtered to delineate the boundaries of the graphene edge of the uppermost plane that were involved in making initial contact with the bacterial cell membrane.

Bacterial Attachment. Two pathogenic, biofilm forming bacteria, *Staphylococcus aureus* CIP 65.8^T and *Pseudomonas aeruginosa* ATCC 9027, both of which are responsible for a significant number of postoperative infections every year, were used in this study.[48,49] *Staphylococcus aureus* CIP 65.8^T and *Pseudomonas aeruginosa* ATCC 9027 were obtained from Culture Collection of the Institute Pasteur (CIP, France) and the American Type Culture Collection (ATCC, USA). Bacterial stocks were prepared in 20% glycerol nutrient broth (Oxoid) and stored at −80 °C until needed. Prior to each experiment, bacterial cultures were refreshed from stocks on nutrient agar (Oxoid) and cells were collected at the logarithmic stage of growth (after 24 h grown in 37 °C). A fresh bacterial suspension was prepared for each of the strains in 20 mL of nutrient broth. Bacterial growth and experimental conditions were according to previously developed protocols.[41,42]

Visualization and quantification of viable bacteria were performed using a FV10i Fluoview (Olympus, Japan) confocal laser scanning microscope (CSLM), operated using the 60× objective lens combined with 3× optical zoom. Bacterial cells were stained with a LIVE/DEAD *Bac*Light Bacterial Viability Kit (Invitrogen); live cells were stained green with SYTO 9 and dead cells were stained red with propidium iodide. Bacteria were counted using ImageJ software using at least six microscope fields at 600× magnification for every sample. The viability of the bacteria was determined as the ratio between the viable and total number of bacteria.

Free Energy Interaction between the Cell Membrane and Graphene. The single-chain mean field (SCMF) theory of lipid bilayers[3,4] provides a detailed description of the mechanical and equilibrium properties of lipid bilayers at the molecular level. Mean fields determine the probabilities of certain conformations of individual molecules being present while the fields are obtained as averages over conformations with their probabilities.[3] Lipid molecules were modeled at a coarse-grained level within the three-beads model,[4] which can adequately describe the compressibility, dimensions of the bilayer, and the equilibrium area per lipid. The lipid molecule is modeled as three freely joint spherical beads of equal radius 4.05 Å and connected by the stiff bond of 10 Å in length. One bead is hydrophilic, and two beads are hydrophobic. The beads interact through square well potentials: between two hydrophobic beads, $\varepsilon_{TT} = 2.1kT$ with the interaction range $r = 12.15$ Å; between one hydrophilic bead and implicit solvent, $\varepsilon_{HS} = -0.15kT$ with an interaction range $r = 12.15$ Å. The solvent molecule in our model is considered to be the same radius as the spherical beads.

Free Energy Calculation. The simulation box of size 300 × 300 × 150 Å was discretized into a 2D cylindrical geometry oriented around the *z*-axis in the center of the simulation box. It is assumed that the simulation box containing one graphene sheet represents a part of a periodic system, which represents a continuous repetition of the simulation box. The periodic boundary conditions were applied in the lateral direction, and a restricted wall was introduced in both the top and bottom of the simulation box. Thus, the free energy of the simulation box can be used to deduce the free energy of the larger periodic system. The total energy of system (F*) can be written as the sum of free energy of solvent (F^*_{box}) and the free energy of the membrane (F^*_{mem}). The number of lipids in the large system is N^*, and the entropy of the pure solvent is $f_s = (\phi_0/V_s)\ln(\phi_0/V_s)$, where v_s is the volume of the solvent and ϕ_0 is the solvent volume fraction. F^* can be rewritten as

$$F^* = F^*_{box} + F^*_{mem} = N^* F_{box} + V_s f_s$$

The free energy cost with respect to the reference state of unperturbed bilayer can be written in the form

$$\Delta F^* = \frac{N^*}{N}F_{box} - \frac{N^*}{N}V_{box}f_s - N^* f_0 + \frac{N^*}{N}V_{obj}f_s$$

where N, F_{box}, and V_{box} denote the number of lipids, total free energy, and the volume of the simulation box. f_0 represents the free energy density of unperturbed bilayer given by the reference state, and V_{obj} is the part of graphene sheet inside the simulation box. We define N/N^* as α:

$$\Delta F = \alpha \Delta F^* = F_{box} - V_{box}f_s - Nf_0 + V_{obj}f_s$$

Conflict of Interest: The authors declare no competing financial interest.

Acknowledgment. We acknowledge Veselin Boshkovikj for making the movie S1. We also acknowledge funding from Marie Curie Actions under EU FP7 Initial Training Network SNAL 608184.

Supporting Information Available: Surface nanoarchitecture transition from graphite to GN-R and GN-S (Movie S1). Figures S1−S5 and Table S1. The Supporting Information is available free of charge on the ACS Publications website at DOI: 10.1021/acsnano.5b03368.

REFERENCES AND NOTES

1. Liu, S.; Zeng, T. H.; Hofmann, M.; Burcombe, E.; Wei, J.; Jiang, R.; Kong, J.; Chen, Y. Antibacterial Activity of Graphite, Graphite Oxide, Graphene Oxide, and Reduced Graphene Oxide: Membrane and Oxidative Stress. *ACS Nano* **2011**, *5*, 6971–6980.
2. Mao, H. Y.; Laurent, S.; Chen, W.; Akhavan, O.; Imani, M.; Ashkarran, A. A.; Mahmoudi, M. Graphene: Promises, Facts, Opportunities, and Challenges in Nanomedicine. *Chem. Rev.* **2013**, *113*, 3407–3424.
3. Novoselov, K. S.; Falko, V. I.; Colombo, L.; Gellert, P. R.; Schwab, M. G.; Kim, K. A Roadmap for Graphene. *Nature* **2012**, *490*, 192–200.
4. Xu, M.; Liang, T.; Shi, M.; Chen, H. Graphene-like Two-Dimensional Materials. *Chem. Rev.* **2013**, *113*, 3766–3798.
5. Hu, W.; Peng, C.; Luo, W.; Lv, M.; Li, X.; Li, D.; Huang, Q.; Fan, C. Graphene-based Antibacterial Paper. *ACS Nano* **2010**, *4*, 4317–4323.
6. Li, J.; Wang, G.; Zhu, H.; Zhang, M.; Zheng, X.; Di, Z.; Liu, X.; Wang, X. Antibacterial Activity of Large-Area Monolayer Graphene Film Manipulated by Charge Transfer. *Sci. Rep.* **2014**, 10.1038/srep04359.
7. Akhavan, O.; Ghaderi, E. Toxicity of Graphene and Graphene Oxide Nanowalls against Bacteria. *ACS Nano* **2010**, *4*, 5731–5736.
8. Gurunathan, S.; Han, J. W.; Dayem, A. A.; Eppakayala, V.; Kim, J.-H. Oxidative Stress-mediated Antibacterial Activity of Graphene Oxide and Reduced Graphene Oxide in *Pseudomonas aeruginosa*. *Int. J. Nanomed.* **2012**, *7*, 5901–5914.
9. Krishnamoorthy, K.; Veerapandian, M.; Zhang, L. H.; Yun, K.; Kim, S. J. Antibacterial Efficiency of Graphene Nanosheets against Pathogenic Bacteria *via* Lipid Peroxidation. *J. Phys. Chem. C* **2012**, *116*, 17280–17287.
10. Tu, Y.; Lv, M.; Xiu, P.; Huynh, T.; Zhang, M.; Castelli, M.; Liu, Z.; Huang, Q.; Fan, C.; Fang, H.; et al. Destructive Extraction of Phospholipids from *Escherichia coli* Membranes by Graphene Nanosheets. *Nat. Nanotechnol.* **2013**, *8*, 594–601.
11. Mangadlao, J. D.; Santos, C. M.; Felipe, M. J. L.; De Leon, A. C. C.; Rodrigues, D. F.; Advincula, R. C. On the Antibacterial Mechanism of Graphene Oxide (GO) Langmuir-Blodgett Films. *Chem. Commun.* **2015**, *51*, 2886–2889.
12. Hui, L.; Piao, J. G.; Auletta, J.; Hu, K.; Zhu, Y.; Meyer, T.; Liu, H.; Yang, L. Availability of the Basal Planes of Graphene Oxide Determines Whether It Is Antibacterial. *ACS Appl. Mater. Interfaces* **2014**, *6*, 13183–13190.
13. Liu, S.; Hu, M.; Zeng, T. H.; Wu, R.; Jiang, R.; Wei, J.; Wang, L.; Kong, J.; Chen, Y. Lateral Dimension-Dependent Antibacterial Activity of Graphene Oxide Sheets. *Langmuir* **2012**, *28*, 12364–12372.
14. Yang, X.; Li, Z.; Ju, E.; Ren, J.; Qu, X. Reduced Graphene Oxide Functionalized with a Luminescent Rare-Earth Complex for The Tracking and Photothermal Killing of Drug-Resistant Bacteria. *Chem. - Eur. J.* **2014**, *20*, 394–398.
15. Akhavan, O.; Ghaderi, E. Photocatalytic Reduction of Graphene Oxide Nanosheets on TiO_2 Thin Film for Photoinactivation of Bacteria in Solar Light Irradiation. *J. Phys. Chem. C* **2009**, *113*, 20214–20220.
16. Sun, H.; Gao, N.; Dong, K.; Ren, J.; Qu, X. Graphene Quantum Dots-Band-aids Used for Wound Disinfection. *ACS Nano* **2014**, *8*, 6202–6210.
17. Shen, J.; Li, T.; Shi, M.; Li, N.; Ye, M. Polyelectrolyte-assisted One-Step Hydrothermal Synthesis of Ag-Reduced Graphene Oxide Composite and Its Antibacterial Properties. *Mater. Sci. Eng., C* **2012**, *32*, 2042–2047.
18. de Faria, A. F.; Martinez, D. S. T.; Meira, S. M. M.; de Moraes, A. C. M.; Brandelli, A.; Filho, A. G. S.; Alves, O. L. Anti-adhesion and Antibacterial Activity of Silver Nanoparticles Supported on Graphene Oxide Sheets. *Colloids Surf., B* **2014**, *113*, 115–124.
19. Santos, C. M.; Tria, M. C.; Vergara, R. A.; Ahmed, F.; Advincula, R. C.; Rodrigues, D. F. Antimicrobial Graphene Polymer (PVK-GO) Nanocomposite Films. *Chem. Commun.* **2011**, *47*, 8892–4.

20. Park, S.; Mohanty, N.; Suk, J. W.; Nagaraja, A.; An, J.; Piner, R. D.; Cai, W.; Dreyer, D. R.; Berry, V.; Ruoff, R. S. Biocompatible, Robust Free-Standing Paper Composed of a TWEEN/Graphene Composite. *Adv. Mater.* **2010**, *22*, 1736–1740.
21. Akhavan, O.; Choobtashani, M.; Ghaderi, E. Protein Degradation and RNA Efflux of Viruses Photocatalyzed by Graphene-Tungsten Oxide Composite under Visible Light Irradiation. *J. Phys. Chem. C* **2012**, *116*, 9653–9659.
22. Kim, S.; Ryoo, S. R.; Na, H. K.; Kim, Y. K.; Choi, B. S.; Lee, Y.; Kim, D. E.; Min, D. H. Deoxyribozyme-loaded Nano-Graphene Oxide for Simultaneous Sensing and Silencing of the Hepatitis C Virus Gene in Liver Cells. *Chem. Commun.* **2013**, *49*, 8241–8243.
23. Li, Y.; Yuan, H.; von dem Bussche, A.; Creighton, M.; Hurt, R. H.; Kane, A. B.; Gao, H. Graphene Microsheets Enter Cells Through Spontaneous Membrane Penetration at Edge Asperities and Corner Sites. *Proc. Natl. Acad. Sci. U. S. A.* **2013**, *110*, 12295–12300.
24. Akhavan, O.; Ghaderi, E.; Esfandiar, A. Wrapping Bacteria by Graphene Nanosheets for Isolation from Environment, Reactivation by Sonication, and Inactivation by Near-infrared Irradiation. *J. Phys. Chem. B* **2011**, *115*, 6279–88.
25. Yi, X.; Gao, H. Cell Interaction with Graphene Microsheets: Near-Orthogonal Cutting *versus* Parallel Attachment. *Nanoscale* **2015**, *7*, 5457–5467.
26. Dallavalle, M.; Calvaresi, M.; Bottoni, A.; Melle-Franco, M.; Zerbetto, F. Graphene can Wreak Havoc with Cell Membranes. *ACS Appl. Mater. Interfaces* **2015**, *7*, 4406–4414.
27. Luan, B.; Huynh, T.; Zhao, L.; Zhou, R. Potential Toxicity of Graphene to Cell Functions *via* Disrupting Protein-Protein Interactions. *ACS Nano* **2015**, *9*, 663–669.
28. Akhavan, O.; Ghaderi, E. *Escherichia coli* Bacteria Reduce Graphene Oxide to Bactericidal Graphene in a Self-limiting Manner. *Carbon* **2012**, *50*, 1853–1860.
29. Notley, S. M. Highly Concentrated Aqueous Suspensions of Graphene Through Ultrasonic Exfoliation with Continuous Surfactant Addition. *Langmuir* **2012**, *28*, 14110–14113.
30. Sham, A. Y. W.; Notley, S. M. A Review of Fundamental Properties and Applications of Polymer-Graphene Hybrid Materials. *Soft Matter* **2013**, *9*, 6645–6653.
31. Tang, Y.; Huang, F.; Zhao, W.; Liu, Z.; Wan, D. Synthesis of Graphene-Supported $Li_4Ti_5O_{12}$ Nanosheets for High Rate Battery Application. *J. Mater. Chem.* **2012**, *22*, 11257–11260.
32. Lu, W.; Liu, S.; Qin, X.; Wang, L.; Tian, J.; Luo, Y.; Asiri, A. M.; Al-Youbi, A. O.; Sun, X. High-yield, Large-scale Production of Few-layer Graphene Flakes Within Seconds: Using Chlorosulfonic Acid and H_2O_2 as Exfoliating Agents. *J. Mater. Chem.* **2012**, *22*, 8775–8777.
33. Hernandez, Y.; Nicolosi, V.; Lotya, M.; Blighe, F. M.; Sun, Z.; De, S.; McGovern, I. T.; Holland, B.; Byrne, M.; Gun'Ko, Y. K.; et al. High-Yield Production of Graphene by Liquid-Phase Exfoliation of Graphite. *Nat. Nanotechnol.* **2008**, *3*, 563–568.
34. Lotya, M.; Hernandez, Y.; King, P. J.; Smith, R. J.; Nicolosi, V.; Karlsson, L. S.; Blighe, F. M.; De, S.; Wang, Z.; McGovern, I. T.; et al. Liquid Phase Production of Graphene by Exfoliation of Graphite in Surfactant/Water Solutions. *J. Am. Chem. Soc.* **2009**, *131*, 3611–3620.
35. Zhu, L.; Zhao, X.; Li, Y.; Yu, X.; Li, C.; Zhang, Q. High-Quality Production of Graphene by Liquid-Phase Exfoliation of Expanded Graphite. *Mater. Chem. Phys.* **2013**, *137*, 984–990.
36. Ni, Z. H.; Wang, H. M.; Ma, Y.; Kasim, J.; Wu, Y. H.; Shen, Z. X. Tunable Stress and Controlled Thickness Modification in Graphene by Annealing. *ACS Nano* **2008**, *2*, 1033–1039.
37. Ferrari, A. C.; Meyer, J. C.; Scardaci, V.; Casiraghi, C.; Lazzeri, M.; Mauri, F.; Piscanec, S.; Jiang, D.; Novoselov, K. S.; Roth, S.; et al. Raman Spectrum of Graphene and Graphene Layers. *Phys. Rev. Lett.* **2006**, *97*, 97.
38. Shinbrot, T.; Muzzio, F. J. Reverse Buoyancy in Shaken Granular Beds. *Phys. Rev. Lett.* **1998**, *81*, 4365–4368.
39. Hong, D. C.; Quinn, P. V.; Luding, S. Reverse Brazil Nut Problem: Competition between Percolation and Condensation. *Phys. Rev. Lett.* **2001**, *86*, 3423–3426.
40. Ivanova, E. P.; Mitik-Dineva, N.; Wang, J.; Pham, D. K.; Wright, J. P.; Nicolau, D. V.; Mocanasu, R. C.; Crawford, R. J. *Staleya guttiformis* Attachment on Poly(*tert*-butylmethacrylate) Polymeric Surfaces. *Micron* **2008**, *39*, 1197–1204.
41. Mitik-Dineva, N.; Wang, J.; Truong, V. K.; Stoddart, P.; Malherbe, F.; Crawford, R. J.; Ivanova, E. P. *Escherichia coli*, *Pseudomonas aeruginosa* and *Staphylococcus aureus* Attachment Patterns on Glass Surfaces with Nanoscale Roughness. *Curr. Microbiol.* **2009**, *58*, 268–273.
42. Truong, V. K.; Rundell, S.; Lapovok, R.; Estrin, Y.; Wang, J. Y.; Berndt, C. C.; Barnes, D. G.; Fluke, C. J.; Crawford, R. J.; Ivanova, E. P. Effect of Ultrafine-Grained Titanium Surfaces on Adhesion of Bacteria. *Appl. Microbiol. Biotechnol.* **2009**, *83*, 925–937.
43. Webb, H. K.; Boshkovikj, V.; Fluke, C. J.; Truong, V. K.; Hasan, J.; Baulin, V. A.; Lapovok, R.; Estrin, Y.; Crawford, R. J.; Ivanova, E. P. Bacterial Attachment on Sub-Nanometrically Smooth Titanium Substrata. *Biofouling* **2013**, *29*, 163–170.
44. Ivanova, E. P.; Truong, V. K.; Webb, H. K.; Baulin, V. A.; Wang, J. Y.; Mohammodi, N.; Wang, F.; Fluke, C.; Crawford, R. J. Differential Attraction and Repulsion of *Staphylococcus aureus* and *Pseudomonas aeruginosa* on Molecularly Smooth Titanium Films. *Sci. Rep.* **2011**, *1*, 165.
45. Akhavan, O.; Ghaderi, E.; Akhavan, A. Size-dependent Genotoxicity of Graphene Nanoplatelets in Human Stem Cells. *Biomaterials* **2012**, *33*, 8017–8025.
46. Akhavan, O.; Ghaderi, E.; Emamy, H.; Akhavan, F. Genotoxicity of Graphene Nanoribbons in Human Mesenchymal Stem Cells. *Carbon* **2013**, *54*, 419–431.
47. Gao, H. Probing Mechanical Principles of Cell-Nanomaterial Interactions. *J. Mech. Phys. Solids* **2014**, *62*, 312–339.
48. Flemming, H. C.; Wingender, J. The Biofilm Matrix. *Nat. Rev. Microbiol.* **2010**, *8*, 623–633.
49. Senneville, E.; Joulie, D.; Legout, L.; Valette, M.; Dezèque, H.; Beltrand, E.; Roselé, B.; D'Escrivan, T.; Loïez, C.; Caillaux, M.; et al. Outcome and Predictors of Treatment Failure in Total Hip/Knee Prosthetic Joint Infections due to *Staphylococcus aureus*. *Clin. Infect. Dis.* **2011**, *53*, 334–340.